Dynamic photophysical processes in laser-irradiated human cortical skull bone measured by means of modulated diffuse luminescence

Andreas Mandelis, Chi-Hang Kwan, and Anna Matvienko
Department of Mechanical and Industrial Engineering, Center for Advanced Diffusion-Wave Technologies, University of Toronto, Toronto, Ontario, Canada M5S 3G8

(Received 5 May 2009; published 19 August 2009)

The technique of modulated luminescence of bones was developed experimentally and theoretically and was subsequently used to interpret measurements performed on the cortical layer of human skull bones. The photophysical theory is based on the optical excitation and decay rate equations of the fluorescent endogenous chromophore and on the molecular interaction parameter with the photon field density in the matrix of the bone. An effective mean relaxation lifetime, τ_M, of skull cortical bone was derived theoretically and was found to depend on the endogenous chromophore decay lifetime, τ_2, in the upper energy state, on the generated luminescence field density through its dependence on the incident photon field density and on the thickness of the bone. A linear dependence of τ_M on laser beam intensity, I_0, was found and sensitivity of the value of τ_M to bone thickness, L, was observed for $L \leq 6.2$ mm. Both experimental dependencies of τ_M on I_0 and L were in excellent agreement with the theoretical model. The unusually long relaxation luminescence lifetime was accounted for theoretically by means of an excited-state manifold invoking intersystem crossing to a forbidden state followed by decay to the ground state of the chromophore. Best fits to the data were able to yield measurements of the following chromophore and photon field parameters: $\tau_2 = 19.7$ ms, optical scattering coefficient $\mu_s(659\ \text{nm}) = 44\,340\ \text{m}^{-1}$, optical absorption coefficient $\mu_a(659\ \text{nm}) = 13\ \text{m}^{-1}$, and coupling coefficient $B_{21} = 1.6 \times 10^4\ \text{m}^3\ \text{J}^{-1}\ \text{s}^{-1}$, the decay coupling coefficient of the endogenous chromophore participating in the optical interaction in the form of stimulated luminescence emission mediated by the luminescence photon field between the long-lived excited state E_2 and the lower (ground) state E_1. The method of modulated luminescence can be used to measure photophysical properties of the chromophore in cortical skull bones, being a sensitive marker of bone diseases, namely, osteoporosis and cancer.

DOI: 10.1103/PhysRevE.80.021920 PACS number(s): 87.10.Ca, 81.70.Fy, 87.15.mq, 87.85.fk

I. INTRODUCTION

Bone is a dynamic living porous mineralized structure consisting of organic components (collagen and long chains of noncollagenous proteins that intertwine in elastic fibers) and inorganic mineral matter in the form of hydroxyapatite, $Ca_{10}(PO_4)_6(OH)_2$, of poor crystalline quality. Mechanically, the ratio of organic matrix to mineral concentration is very important. Newly deposited bone is low in mineral density. As mineral density increases and bone crystals increase in size, the stiffness of bone increases [1]. Bone crystallinity is also a measure of turnover rate, where the average crystal size is smaller in young bone because newly formed crystals are smaller than mature crystals. Bone mineral crystals are colloidal in size, so there is a large amount of surface area on which normal lattice ions can be substituted by other ions in solution. The calcium site can be substituted by [2] Na^+, K^+, Mg^{2+}, Sr^{2+}, and Pb^{2+} and the anionic sites can be substituted with CO_3^{2-}, HPO_4^{2-}, Cl^-, and F^-. These substitutions into the hydroxyapatite lattice are very important to bone strength, flexibility, and the process of remodeling. This structure is constantly undergoing renewal processes as old material is removed and new added.

Investigations of the optical properties of human bones have been growing rapidly in recent years as a result of the perceived need to develop new diagnostic tools to combat the increased incidence of osteoporosis (OP), a major public health problem, especially in aging populations: in the U.S. alone 10 million persons (mostly postmenopausal Caucasian women) have osteoporosis and 18 million more have low bone mass, a condition known as *osteopenia* [3]. Miller *et al.* [4] have used far infrared fluorescence spectroscopy of tibia bones from ovariectomized female monkeys (potentially during the onset of postovariectomy OP) and reported sensitivity of several substitutional mineral absorption bands to mineral content, crystallinity, and the content/nature of the organic matrix. Takeuchi *et al.* [5] have performed preliminary measurements of elastic optical-range light scattering from the hydroxyapatite of bone and they found a correlation between optical attenuation and bone mineral density (BMD). This sets the stage for a noninvasive BMD measurement technique. Recently Ugryumova *et al.* [6] used white light, an integrating-sphere and optical coherence tomography (OCT) to perform diffuse reflectance and transmittance measurements of intentionally demineralized cortical horseleg bone over the spectral range of 520–960 nm. An approximately linear relationship between scattering coefficient, μ_s, ($\sim 25-35\ \text{mm}^{-1}$) and BMD was found and attributed to the presence of hydroxyapatite crystals. Values of the optical absorption coefficient, μ_a, spectra were $\leq 0.12\ \text{mm}^{-1}$ and also exhibited strong decreases with increasing demineralization, as well as a directional dependence of the optical absorption coefficient on bone anisotropy controlled by collagen fiber orientation. This is an important result as it shows the feasibility of optical absorption- and scattering-based bone loss diagnostic probes. Similar effects were reported during mid-infrared measurements of human trabecular bone using a Fourier-transform infrared (FTIR) spectrometer [7].

By way of OP quantification, the World Health Organization (WHO) proposed diagnostic guidelines for OP [8,9] based on the measurement of BMD by dual energy x-ray absorptiometry (DXA or DEXA), the major diagnostic technique to date [10–12]. Besides DEXA, the following bone densitometry techniques are currently used for density measurements of bone: quantitative computed tomography, radiographic absorptiometry, peripheral quantitative computed tomography, quantitative ultrasound (Q-US), and quantitative measurements of trabecular bone through magnetic resonance images [13]. Purely ultrasonic techniques such as Q-US use the attenuation of nonionizing ultrasound waves and changes in the speed of sound to diagnose variations in bone density and osteoporosis. However, a wide acoustic frequency range is required [14], i.e., large transducer arrays, which affect spatial resolution. Intimate contact with the bone is required which may be inconvenient for nonflat body areas and compromises signal reproducibility. Besides the aforementioned experimental limitations, a potential practical drawback is the complexity of the interaction mechanisms between the incident ultrasonic field and the bone [15]. This issue adds nonspecificity to purely ultrasonic measurements which are not yet fully understood.

The foregoing overview of wave-based bone diagnostic techniques shows or implies that there are measurable differences in bone optical and acoustic properties, with optical excitation providing superior specificity to that of the low-contrast ultrasound. Therefore, the investigation of the response of bone to optical stimuli may be important toward the development of sensitive diagnostic techniques of the onset of OP at the very earliest stage and for detailed characterization of bone matter without the ionizing effects of x rays. Modulated luminescence (LUM) of hard tissues is a method which is based on direct near-infrared radiative photon emissions from chromophores responding to optical excitation. Our preliminary measurements on human cranial vault (skull) bones [16] have revealed strong luminescence emission with modulation frequency dependence very similar to that exhibited by dental enamel luminescence characteristic of hydroxyapatite [17]. Mineral loss was simulated using 37% phosphoric acid gel (3M ESPE AG, Scotchbond™) and was validated using transverse microradiography. An etching treatment series was done sequentially with LUM signals measured before and after each treatment time. The luminescence amplitude and phase showed very small differences which, however, were measurable due to the very high signal stability and signal-to-noise ratio (SNR; several hundred). Bone luminescence emission was observed in the 700–850 nm range, generally the same spectral range as hydroxyapatite [18] which has approx 1 cm optical absorption length and is thus very sensitive to the value of the optical absorption coefficient, μ_a. The observed high SNR implies that synchronous lock-in detection of laser-source-filtered LUM can be used to easily detect minute changes in bone texture by means of sensitive photodetectors, e.g., Si or InGaAs. LUM signals can subsequently be linked to intrinsic bone photophysical properties, a major goal of this paper. A fundamental understanding of bone photophysics can thus be obtained and used to introduce and quantify two-dimensional LUM imaging using laser scanning or near-infrared cameras.

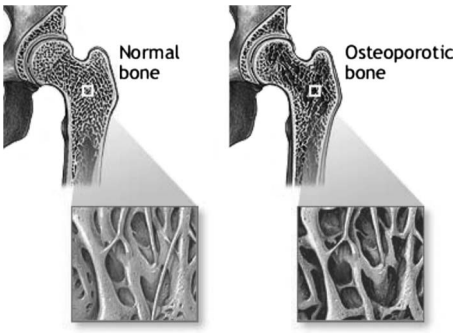

FIG. 1. Solid and osteoporotic bone matrix of a hip bone (http://www.nlm.nih.gov/medlineplus/ency/imagepages/17285.htm).

The dependence of the modulated LUM signal on the optical properties of bones (absorption and scattering coefficients) renders this technique sensitive to minute *geometrical* changes in bone, e.g., the void fraction, due to density changes (Fig. 1). In addition, the optical-to-radiative energy conversion associated with modulated luminescence is shown to be sensitive to *intrinsic* photophysical properties of endogenous LUM generating bone chromophore(s). The combination of these factors may potentially act additively to render LUM an optimal noninvasive diagnostic technique capable of detecting the onset of bone density changes and osteoporosis at the earliest stages. In this paper we construct a photophysical theoretical model of LUM to explain its dependence on the optical properties of the bone and of the experimentally observed endogenous chromophore excited-state relaxation lifetime in the bulk (matrix) of the skull. We use the model to measure the dependence of modulated luminescence of human cortical skull bone on the excitation laser beam modulation frequency. In the next section we put forth a photophysical theoretical model based on the diffuse luminescence field present in skull cortical bone considered as a turbid medium.

II. MODULATED LUMINESCENCE PHOTOPHYSICS OF BONE

A. Exact rate theory

It is well known that endogenous fluorophores such as collagen in bone exhibit typical fluorescence lifetimes on the order of nanoseconds or shorter. However, the luminescence emission observed in the reported measurements has a very long lifetime (ms). Therefore one is led to conclude that a simple two-state model of the excited-state energy manifold of the luminescent endogenous chromophore in cortical human skull bones [16] is not an accurate depiction of the photophysical processes occurring upon optical excitation, but instead a forbidden transition associated with intersystem crossing of is a more likely process, as shown in Fig. 2. Given that little is known about the photophysics of this newly observed luminescence emission from skull bone, the formalist will be kept as general as possible and the theoretical predictions will be applied to the data. $W_{pv}(t)$ is the optical pump rate represented by the laser beam which excites the chromophore in the skull bone to the upper inter-

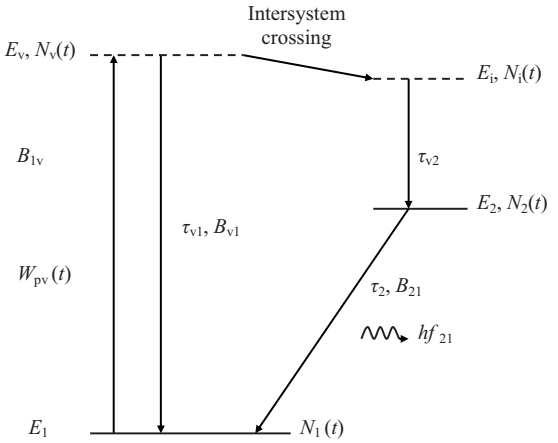

FIG. 2. Bone chromophore excitation manifold involving intersystem crossing into a state E_i from a virtual excited state E_v. A forbidden transition from the vertical-decay cross state E_2 to the ground state takes place stimulated by the presence of the luminescence field in the luminescence-reabsorption dynamic model.

mediate (virtual) state E_v. The chromophore on this level crosses into the virtual level E_i and eventually decays into the upper state E_2 of the observed transition either as heat (nonradiatively) or radiatively with effective lifetime τ_{v2}. Once in state E_2 the chromophore decays as the observed luminescence photon emission. The characteristic decay time from energy level 2 to 1 is denoted as τ_2. The fact that the direct pathway $E_v \rightarrow E_1$ is also possible and very likely determines the relative populations in states 2 and 1 proportionately to the decay times of E_v and E_2 into the ground state E_1. The lifetime τ_{v1} associated with the direct deexcitation pathway is typically assumed to be on the order of ~ns. Upon incidence of laser light on the surface of the hard turbid tissue of the cortical bone, a diffuse photon field is established in the bulk of the bone, Fig. 3, past the ballistic photon range. The bone matrix is assumed to have optical absorption coefficient $\mu_a(\lambda)$ and scattering coefficient $\mu_s(\lambda)$, Fig. 3. Here λ is the wavelength of the excitation laser beam. The presence of the laser field of wavelength λ in the matrix results in the optical density $\rho(z,\lambda,\omega)$[J m^{-3}],

$$\rho(z,\lambda;\omega) = \frac{1}{2}\rho_0(z,\lambda)(1+e^{i\omega t}), \tag{1}$$

where $\omega=2\pi f$ is the angular modulation frequency of the excitation laser intensity I_0. The three-dimensional nature of the optical density field $\rho=\rho_0(r,\theta,z;\lambda,\omega)$ has been suppressed and simplified into a one-dimensional (1D) field ρ

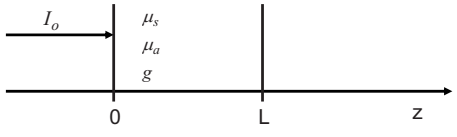

FIG. 3. A cross-sectional view of the model geometry. I_0: intensity of the incident laser radiation; L: bone thickness; μ_a: optical absorption coefficient; μ_s: optical scattering coefficient; g: mean cosine of the scattering angle.

$=\rho_0(z,\lambda;\omega)$ because (a) the skull bones dealt with in this research exhibited essentially isotropic optical behavior (θ independent) and (b) the profuse optical scattering in the skull matrix broadened the extent of the field considerably beyond the radius of the excitation laser beam spot size, thereby rendering the luminescence frequency response essentially independent of the radial coordinate within the approx (50 μm)^2 viewing area of the near-infrared detector of the emitted luminescence. In any case, in the theoretical model it will be seen that the spatial integral of the optical field does not affect the details of the frequency response of the modulated luminescence. The relation between the optical density and total photon field Ψ_t in the turbid medium is [19]

$$\rho(z,\lambda;\omega) = \frac{1}{c}\Psi_t(z,\lambda;\omega),$$

$$\Psi_t(z,\lambda;\omega) = \Psi_d(z,\lambda;\omega) + \Psi_c(z,\lambda;\omega), \tag{2}$$

where Ψ_d and Ψ_c are the diffuse and coherent components of the total optical field in the bone matrix, respectively [19]. The latter component largely accounts for optical propagation within the ballistic photon regime (ca. 50 μm from the surface) [20]. The photophysical picture evoked in this model to interpret the LUM data is one in which the photon density field induces luminescence through deexcitations in the chromophore and luminescence photons, in turn, stimulate further decay of the chromophore in the excited state E_2 cross-linked to the ground state E_1 through a forbidden transition with long lifetime τ_2. The number density of stimulated deexciting chromophores depends on the optical (and generated luminescence) intensity in their neighborhood and is a function of depth, following optical absorption, scattering, and attenuation in the turbid medium. Therefore, the dynamic stimulation parameters of the decay process to the ground state are functions of depth in the bone. This process occurs in parallel with the spontaneous decay of the excited molecular system which is characterized by the lifetime τ_2. At the same time the direct deexcitation process $E_v \rightarrow E_1$ is also occurring very efficiently, thus returning the majority of the excited chromophores to the ground state via this route with relaxation time τ_{v1}, the competing process being the crossover one with decay lifetime τ_{v2}. In keeping with the 1D approximation, the excited-state concentration of luminescent molecules $N_2(z,\omega)$ is the source of the LUM signal at mean wavelength $\lambda_{LUM}=c/f_{21}$, where f_{21} is the mean optical frequency of the emitted luminescence and $c=c_0/n$ is the speed of light in skull cortical bone; c_0 is the speed of light in the vacuum and n is the refractive index of bone:

$$Q(z,\lambda_{LUM};\omega) = \eta_R h f_{21} N_2(z;\omega) \quad [\text{J m}^{-3}], \tag{3}$$

where η_R is the radiative energy conversion efficiency and h is Planck's constant.

The rate equations for the populations in the excited-state manifold, including the intermediate state, are $N_v(z,\omega)$, $N_1(z,\omega)$, and $N_2(z,\omega)$ respectively. They can be written as

$$\frac{\partial N_v(z;\omega)}{\partial t} = -(B_{v1}/c)\Psi_t(z;\omega)N_v(z;\omega) - \left(\frac{1}{\tau_{v1}} + \frac{1}{\tau_{v2}}\right)N_v(z;\omega) + (B_{1v}/c)\Psi_t(z;\omega)N_1(z;\omega), \tag{4a}$$

$$\frac{\partial N_2(z;\omega)}{\partial t} = \frac{N_v(z;\omega)}{\tau_{v2}} - (B_{21}/c)\Psi_t(z;\omega)N_2(z;\omega) - \frac{1}{\tau_2}N_2(z;\omega), \tag{4b}$$

$$\frac{\partial N_1(z,\omega)}{\partial t} = (B_{v1}/c)\Psi_t(z;\omega)N_v(z;\omega) + (B_{21}/c)\Psi_t(z;\omega)N_2(z;\omega) + \frac{N_v(z;\omega)}{\tau_{v1}} + \frac{N_2(z;\omega)}{\tau_2} - (B_{1v}/c)\Psi_t(z;\omega)N_1(z,\omega). \tag{4c}$$

Here the excitation wavelength, λ dependence of the total optical field Ψ_t was suppressed. The product $(B_{ij}/c)\Psi_t$ is the probability per unit frequency that optical transitions are induced by the diffuse luminescence field from level i to level j. Figure 2 depicts the intersystem crossing and decay to the state E_2 of the arbitrary excited state E_v populated by the optical pump field $W_{p2}(\lambda,\omega)$. Luminescence photons of energy $\Delta E=E_2-E_1=hf_{21}$ are emitted. E_1 is the chromophore ground state. Alternatively, the ground state may be a different energy level labeled E_0 not shown in Fig. 2. $B_{ij}[\mathrm{m^3\ J^{-1}\ s^{-1}}]$ are the optical coupling coefficient between levels i and j. c is the speed of light in the medium. Adding Eqs. (4a)–(4c) one can readily show that $\frac{\partial}{\partial t}[N_v(z;\omega)+N_2(z;\omega)+N_1(z;\omega)]=0$, i.e., the overall chromophore density is constant: $N_v(z;\omega)+N_2(z;\omega)+N_1(z;\omega)=\text{const}=N_t(z;\omega)$. The total number of chromophores in a bone sample is fixed and this leads to the molecular concentration conservation condition,

$$\int_0^L N_1(z;\omega)dz + \int_0^L N_2(z;\omega)dz + \int_0^L N_v(z;\omega)dz = N_tL = \text{const}, \tag{5}$$

where N_t is the (uniform) total concentration of all chromophores (all states) at any depth z. Since there is no spatial transport of chromophores, instead of Eq. (5) a local conservation principle will apply at all coordinate points z within the turbid medium:

$$N_1(z;\omega) + N_2(z;\omega) + N_v(z;\omega) = N_t(z;\omega) \equiv N_t. \tag{6}$$

The coupling of the two assumed states (1) and (2) in the bone matrix by means of rate equations (4) mixes the modulated total optical field,

$$\Psi_t(z;\omega) = \frac{1}{2}\Psi_{t0}(z)(1+e^{i\omega t}), \tag{7}$$

with the full Fourier spectrum of the chromophore molecules at all states,

$$N_j(z;\omega) = \sum_{k=0}^{\infty} N_{jk}(z)e^{ik\omega t}, \quad j=1,2,v, \tag{8}$$

where $k=0$ denotes the dc component of the N_j molecular distribution. Given that the experimental system only monitors the fundamental component $(k=1)$ of each molecular excited state because the lock-in amplifier filters out the dc baseline and all other harmonics, Eqs. (7) and (8) can be inserted in Eq. (4) and the various harmonic orders $O(e^{ik\omega t})$ can be calculated. Each harmonic order, $k\omega$, and the one higher, $(k+1)\omega$, are coupled through an infinite system of algebraic equations, the result of equating terms of the same harmonic order on the left- and right-hand sides of Eq. (4). The set of coupled rate equations (4) actually reduces to two, Eqs. (4b) and (4c), as $N_v(z;\omega)=N_t-N_1(z;\omega)-N_2(z;\omega)$ from the conservation conditions. The contribution of N_2 in the form of the Fourier component N_{2k} in each order is used as an input to the next higher harmonic order. Thus, the dc components of the excited-state concentration $N_2(z,\omega)$ and $N_1(z;\omega)$ are calculated from the dc terms in Eqs. (4b) and (4c):

$$\left[\left(\frac{B_{21}}{2c}\right)\Psi_{t0}(z) + \frac{1}{T_2}\right]N_{20}(z) = \frac{1}{\tau_{v2}}[N_t - N_{10}(z)], \tag{9a}$$

$$\left[\left(\frac{B_{v2}}{c}\right)\Psi_{t0}(z) + \frac{1}{T_v}\right]N_{20}(z) = \left[\left(\frac{B_{v1}}{2c}\right)\Psi_{t0}(z) + \frac{1}{\tau_{v1}}\right]N_t - \left[\left(\frac{\overline{B_{1v}}}{c}\right)\Psi_{t0}(z) + \frac{1}{\tau_{v1}}\right]N_{10}(z). \tag{9b}$$

Here the following definitions were made:

$$\overline{B_{1v}} \equiv \frac{1}{2}(B_{1v}+B_{v1}),$$

$$B_{v2} \equiv \frac{1}{2}(B_{v1}-B_{21}),$$

$$T_v \equiv \left(\frac{1}{\tau_{v1}} - \frac{1}{\tau_2}\right)^{-1},$$

$$T_2 \equiv \left(\frac{1}{\tau_{v2}} + \frac{1}{\tau_2}\right)^{-1}. \tag{10}$$

In addition, we may define the following transition rates (see Fig. 2):

$$R_1(z) \equiv \left(\frac{B_{21}}{2c}\right)\Psi_{t0}(z) + \frac{1}{T_2},$$

$$R_2(z) \equiv \left(\frac{B_{v2}}{c}\right)\Psi_{t0}(z) + \frac{1}{T_v},$$

$$R_3(z) \equiv \left(\frac{\overline{B_{1v}}}{c}\right)\Psi_{t0}(z) + \frac{1}{\tau_{v1}},$$

$$R_4(z) \equiv \left(\frac{B_{v1}}{2c}\right)\Psi_{t0}(z) + \frac{1}{\tau_{v1}}. \tag{11}$$

The solution of the algebraic system [Eqs. (9a) and (9b)] leads to the following expressions for the dc populations:

$$N_{10}(z) = N_t\left[\frac{\tau_{v2}R_1(z)R_4(z) - R_2(z)}{\tau_{v2}R_1(z)R_3(z) - R_2(z)}\right] \tag{12a}$$

and

$$N_{20}(z) = N_t\left[\frac{(B_{1v}/2c)\Psi_{t0}(z)}{\tau_{v2}R_1(z)R_3(z) - R_2(z)}\right]. \tag{12b}$$

It is important to note that setting $\Psi_{t0}(z)=0$ in the foregoing expressions results in $N_{10}(z)=N_t$ and $N_{20}(z)=0$, as expected. Also, when $\Psi_{t0}(z)>0$, but, $\tau_{v1}^{-1} \gg K\Psi_{t0}(z)$, then, again, $N_{10}(z)\approx N_t$ as the vast majority of the excited chromophore molecules returns to the ground state through the direct (vertical) deexcitation pathway.

Now, equating the $O(e^{i\omega t})$ terms on both sides of Eqs. (4b) and (4c) yields algebraic equations which involve the dependence of the Fourier components $N_{11}(z;\omega)$ and $N_{21}(z;\omega)$ on $N_{10}(z)$ and $N_{20}(z)$:

$$[i\omega + R_1(z)]N_{21}(z;\omega) = -\frac{N_{11}(z;\omega)}{\tau_{v2}} - \left(\frac{B_{21}}{2c}\right)\Psi_{t0}(z)N_{20}(z), \tag{13a}$$

$$[i\omega + R_3(z)]N_{11}(z;\omega) = -R_2(z)N_{21}(z;\omega) + \left(\frac{B_{v1}}{2c}\right)\Psi_{t0}(z)N_t - \left(\frac{\overline{B_{1v}}}{c}\right)\Psi_{t0}(z)N_{10}(z) - \left(\frac{B_{v2}}{c}\right)\Psi_{t0}(z)N_{20}(z). \tag{13b}$$

After considerable manipulation, the solution for the experimentally significant population $N_{21}(z;\omega)$ can be written in the form

$$N_{21}(z;\omega) = N_t\Psi_{t0}(z)\left\{\left\{\left(\frac{\overline{B_{1v}}}{c}\right)\left[\frac{\tau_{v2}R_1(z)R_4(z) - R_2(z)}{\tau_{v2}R_1(z)R_3(z) - R_2(z)}\right] + \left(\frac{B_{v2}}{2c}\right)\left[\frac{(B_{1v}/c)\Psi_{t0}(z)}{\tau_{v2}R_1(z)R_3(z) - R_2(z)}\right] - \left(\frac{B_{v2}}{2c}\right)\right\} \Big/ [\tau_{v2}(i\omega + R_3(z))] - \frac{1}{4}\left(\frac{B_{21}}{2c}\right)\left[\frac{(B_{1v}/c)\Psi_{t0}(z)}{\tau_{v2}R_1(z)R_3(z) - R_2(z)}\right]\right\} \times \left\{i\omega + R_1(z) - \frac{R_2(z)}{\tau_{v2}[i\omega + R_3(z)]}\right\}^{-1}. \tag{14}$$

This general formula can be significantly simplified using the fact that vertical fluorescence transitions take place at times very short compared to our experimental luminescence frequency probe, i.e., one may set $\tau_{v1} \ll \tau_2$. In this limit $T_v \sim \tau_{v1}$; $(\frac{B_{lm}}{c})\Psi_{t0}(z) + \frac{1}{\tau_{v1}} \approx \frac{1}{\tau_{v1}}$ for any state coupling constant B_{lm}. This implies

$$\begin{aligned}\tau_{v2}R_1(z)R_4(z) - R_2(z) &\approx \tau_{v2}R_1(z)R_3(z) - R_2(z) \\ &\approx (\tau_{v2}/\tau_{v1})\left[\left(\frac{B_{21}}{2c}\right)\Psi_{t0}(z) + \frac{1}{\tau_2}\right].\end{aligned} \tag{15}$$

Now Eq. (12b) for the dc population of state E_2 can be simplified:

$$N_{20}(z) \simeq N_t\left(\frac{\tau_{v1}}{\tau_{v2}}\right)\left[\frac{(B_{1v}/2c)\Psi_{t0}(z)}{(B_{21}/2c)\Psi_{t0}(z) + \tau_2^{-1}}\right]. \tag{16}$$

Similarly, Eq. (14) for the population of state E_2 modulated at the fundamental frequency $f=\omega/2\pi$ can be simplified considerably using the foregoing approximations. In addition, the approximation $i\omega + R_3(z) \sim 1/\tau_{v1}$ is used for modulation frequencies in the range of our experiments (≤ 1 kHz) and the rate

$$R_5(z) \equiv \left(\frac{B_{21}}{2c}\right)\Psi_{t0}(z) + \frac{1}{\tau_2} \tag{17}$$

is defined. Then

$$N_{21}(z;\omega) = N_t\left(\frac{\tau_{v1}}{\tau_{v2}}\right)\left[\frac{\tau^2(z)\Psi_{t0}(z)}{1 + i\omega\tau(z)}\right]\left(\frac{B_{1v}}{2c}\right)\left\{R_5(z) + \left[\left(\frac{\tau_{v1}}{\tau_{v2}}\right) \times \left(\frac{B_{v2}}{c}\right) - \left(\frac{B_{21}}{2c}\right)\right]\Psi_{t0}(z)\right\}. \tag{18}$$

Taking into account that the theoretical best fits to our experimental data yield values $(B_{1v}/c) \sim 10^{-3}$ m^3 J^{-1} s^{-1}, we may ignore the products $(B_{1v}/2c)(B_{v2}/c)$ and $(B_{1v}/2c)(B_{21}/2c)$. This yields the simplified equation

$$N_{21}(z;\omega) \simeq N_t\left(\frac{\tau_{v1}}{\tau_{v2}}\right)\left[\frac{(B_{1v}/2c)\tau(z)\Psi_{t0}(z)}{1 + i\omega\tau(z)}\right]. \tag{19}$$

Here, a depth-dependent effective relaxation time constant $\tau(z)=1/R_5(z)$ was defined as follows:

$$\frac{1}{\tau(z)} \equiv \frac{1}{\tau_2} + (B_{21}/2c)\Psi_{t0}(z). \tag{20}$$

Physically, $\tau(z)$ represents the combined effect of spontaneous and luminescence-field-induced chromophore forbidden transition from the intersystem crossed upper excited state E_2

to the lower state E_1. The modulated population of the exited state $N_{21}(z;\omega)$ depends on the branching ratio of deexcitation lifetimes between the direct vertical transition $E_v \rightarrow E_1$ and the indirect (and much slower) transition $E_v \rightarrow E_2 \rightarrow E_1$. The decay time also depends on the coupling coefficient B_{21} as expected. The luminescence photon density of energy $\Delta E = hf_{21}$, in turn, is the result of the presence of the laser excitation field $\Psi_{t0}(z)$ which populates (one or more) states E_v contributing to the population of E_2. Therefore, as the optical (and luminescence) field density varies across the thickness of the bone matrix, so does the value of τ. If the external optical field is switched off, τ reduces to the intrinsic decay time constant τ_2 characteristic of the molecular excited state of the chromophore. When the external optical field is present, the total decay time constant decreases proportionately to the field intensity as expected from stimulated emission. From Eqs. (3) and (19) the measured LUM signal at the fundamental frequency $f=\omega/2\pi$ is given by

$$S(\omega) = \text{const} \int_0^L N_{21}(z;\omega)dz = \text{const} \int_0^L \frac{\tau(z)\Psi_{t0}(z)dz}{1+i\omega\tau(z)}. \tag{21}$$

It should be noted that if the three-dimensional character of the laser excitation photon field were fully taken into account in the model, i.e., $\Psi_{t0}=\Psi_{t0}(r,z)$, the Hankel integral of the form $\Psi_{t0}(r,z)=\int_0^\infty \tilde{\Phi}_{t0}(k,z)J_0(kr)kdk$ would have to replace $\Psi_{t0}(z)$ in Eq. (21). Here $\tilde{\Phi}_{t0}(k,z)$ and $J_0(kr)$ are the Hankel transform of $\Psi_{t0}(r,z)$ and the Bessel function of the first kind of order zero, respectively [19]. This is a more complicated expression, however, it does not alter the modulation frequency dependence of the emitted luminescence which only appears in the denominator of the integral in Eq. (21). This mathematical argument shows why the dimensionality of the modulated luminescence response in Eq. (21) is not an issue in studies of the frequency response of the LUM field emitted from skull bones.

The result of Eq. (21) with or without the radial dependence of Ψ_{t0} is exact provided $\tau_{v1} \ll \tau_2$, however, the integral does not have an analytical solution and is difficult to use for fitting purposes of the theory to the data due to the complexity of the optical field expression for $\Psi_{t0}(z)$. Therefore, an approximation is introduced to the general theory which allows for further comparison with the experimental results.

B. Approximate mean-value rate theory

The dc terms in Eqs. (4b) and (4c) lead to the expression for $N_{10}(z)$ and $N_{20}(z)$, Eqs. (9a) and (9b). Integrating over the thickness of the bone matrix yields

$$\frac{1}{T_2}\int_0^L N_{20}(z)dz + \left(\frac{B_{21}}{2c}\right)\int_0^L \Psi_{t0}(z)N_{20}(z)dz = \left(\frac{L}{\tau_{v1}}\right)N_t - \frac{1}{\tau_{v2}}\int_0^L N_{10}(z)dz \tag{22a}$$

and

$$\left(\frac{\overline{B_{1v}}}{c}\right)\int_0^L \Psi_{t0}(z)N_{10}(z)dz + \frac{1}{\tau_{v1}}\int_0^L N_{10}(z)dz = \left(\frac{L}{\tau_{v1}}\right)N_t + \left(\frac{B_{v1}}{2c}\right)N_t\int_0^L \Psi_{t0}(z)dz - \frac{1}{T_v}\int_0^L N_{20}(z)dz - \left(\frac{B_{v2}}{c}\right)\int_0^L \Psi_{t0}(z)N_{20}(z)dz. \tag{22b}$$

The approximation involves equating two definitions of the mean value of the dc terms of the excited endogenous chromophore

$$\langle N_{j0}\rangle = \frac{\int_0^L \Psi_{t0}(z)N_{j0}(z)dz}{\int_0^L \Psi_{t0}(z)dz} \simeq \frac{1}{L}\int_0^L N_{j0}(z)dz, \quad j=1,2, \tag{23}$$

which is valid for turbid media where slowly spatially attenuated photon fields can be established. Using these definitions in Eqs. (22a) and (22b), after some manipulation one obtains the mean-value counterpart of Eq. (12b):

$$\langle N_{20}\rangle = N_t\left(\frac{R_{3M}-R_{4M}}{\tau_{v2}R_{1M}(R_{3M}-R_{2M})}\right) \tag{24}$$

and a similar expression for Eq. (12a). Here the mean-value counterparts of Eq. (11) were defined as follows:

$$R_{1M} \equiv \left(\frac{B_{21}}{2c}\right)\langle\Psi_{t0}\rangle + \frac{1}{T_2},$$

$$R_{2M} \equiv \left(\frac{B_{v2}}{c}\right)\langle\Psi_{t0}\rangle + \frac{1}{T_v},$$

$$R_{3M} \equiv \left(\frac{\overline{B_{1v}}}{c}\right)\langle\Psi_{t0}\rangle + \frac{1}{\tau_{v1}},$$

$$R_{4m} \equiv \left(\frac{B_{v1}}{2c}\right)\langle\Psi_{t0}\rangle + \frac{1}{\tau_{v1}}. \tag{25}$$

Using the approximations $\tau_{v1} \ll \tau_2$ and $(B_{lm}/c)\langle\Psi_{t0}\rangle + 1/\tau_{v1} \approx 1/\tau_{v1}$ yields

$$\langle N_{20}\rangle = N_t(\tau_{v1}/\tau_{v2})(B_{1v}/2c)\tau_M\langle\Psi_{t0}\rangle, \tag{26}$$

where

$$\frac{1}{\tau_M} \equiv \frac{1}{\tau_2} + \left(\frac{B_{21}}{2c}\right)\langle\Psi_{t0}\rangle. \tag{27}$$

Similarly, the contribution of the excited-state chromophore molecules to the fundamental Fourier component, Eqs. (13a) and (13b), can be integrated in the mean-value sense. The results are in a compact form:

$$(i\omega + R_{1M})\langle N_{21}\rangle = -\frac{\langle N_{11}\rangle}{\tau_{v2}} - \left(\frac{B_{21}}{2c}\right)\langle N_{20}\rangle\langle\Psi_{t0}\rangle, \tag{28a}$$

$$(i\omega + R_{3M})\langle N_{11}\rangle = N_t\left[\left(\frac{B_{v1}}{2c}\right) - \left(\frac{\overline{B_{1v}}}{c}\right)\left(\frac{R_{4M}}{R_{3M}}\right)\right]\langle \Psi_{t0}\rangle + \left[\left(\frac{\overline{B_{1v}}}{c}\right)\left(\frac{R_{2M}}{R_{3M}}\right) - \left(\frac{B_{v2}}{c}\right)\right]\langle N_{20}\rangle\langle \Psi_{t0}\rangle - R_{2M}\langle N_{21}\rangle. \quad (28b)$$

From these two equations and the mean-value approximations above, a simplified mean-value expression for $\langle N_{21}(\omega)\rangle$ may be obtained:

$$\langle N_{21}(\omega)\rangle = N_t\left(\frac{\tau_{v1}}{\tau_{v2}}\right)\left[\frac{(B_{1v}/2c)\tau_M\langle \Psi_{t0}\rangle}{1 + i\omega\tau_M}\right]. \quad (29)$$

This expression bears resemblance to the local Eq. (19), however, it involves the mean optical field value $\langle \Psi_{t0}\rangle$ and definition of the effective excited-state lifetime τ_M, Eq. (27).

The derived expression (29) is relatively simple and physically transparent. It involves the expected state-coupling constants B_{1v} which allows for chromophore molecule excitation by the optical pump and B_{21}, which allows coupling to the ground state from level E_2 as the means of producing delayed luminescence photons as a fraction of the originally excited chromophore controlled by the branching ratio (τ_{v1}/τ_{v2}). However, there is an important limitation in the definition of effective lifetime τ_M due to its mean-value nature stemming from the equality of the two definitions of mean value embedded in the assumed equivalence (23). The usual definition of an "average" value $\langle \Psi_{t0}(L)\rangle = \frac{1}{L}\int_0^L \Psi_{t0}(z)dz$ assigns decreasing values of the generated optical and luminescence photon density fields as thickness increases. For thin nonscattering slabs optical confinement in the slab determined by mismatch of optical properties and reflections at the boundaries (especially the back boundary) *increases* optical (and expected luminescence density) with *decreasing* thickness. This is not the case with strongly scattering turbid media, such as bone slabs, for two reasons: (1) the diffuse component of the optical excitation and luminescence fields does not allow efficient optical confinement at the back interface, with the result that thinner slabs undergo a much more significant loss of optical flux through the back interface which steepens the density gradient inward from the interface and decreases the overall photon density. This will result in weakening of the luminescence density in the body of the skull bone with thinner slabs or increasing the photon density wit thicker slabs. (2) Related to the scattering nature of the medium, if two slabs of thickness $L_1 < L_2$ are irradiated identically, and one considers a virtual slice of thickness $0 < z_0 < L_1$ in both slabs, the photon density within the thickness $z < z_0$ will be higher in the case of the thicker slab L_2 because $z > z_0$ regions contribute more backscattered photons into the $z \le z_0$ region, thus *increasing* the photon density with *increasing* slab thickness; the thicker the slab the larger the contribution and the higher the photon density. Given the attenuating character of the absorbing and scattering field, the backscattered photon density is expected to saturate at large thicknesses L compared to the optical extinction length in the turbid medium. Both effects (1) and (2) are synergistic and have been observed in our measurements with bone thickness as a parameter. These physical effects including depth saturation are captured by the diffuse photon density theory developed in Sec. II B, but the usual definition of mean value which includes the $1/L$ factor is inconsistent with the turbid character of the medium, so a different normalization factor other than thickness was sought for this expression. It will be noted that if the exact definition, Eq. (20), of the effective deexcitation lifetime is allowed, no thickness scale $1/L$ enters the integral of the optical field $\Psi_{t0}(z)$ and the mathematical form of this function (see below) allows for a correct description of the phenomena.

To remain consistent with the mean-value approximation and calculate a physically acceptable mean value $\langle \Psi_{t0}\rangle$, the following definition of "mean" is used:

$$\langle \Psi_{t0}(L)\rangle = \frac{1}{D}\int_0^L \Psi_{t0}(z)dz, \quad (30)$$

where D is the characteristic optical extinction depth where the photon density field drops to the $1/e$ of its surface value. The value of $\langle \Psi_{t0}(\infty)\rangle$ in the limit of a semi-infinite turbid medium (or of a medium thickness large enough so that back-propagated photon contribution saturation to the total number density of local photons will occur) can be used to normalize the value for the finitely thick medium:

$$\langle \Psi_{t0}(L)\rangle = \langle \Psi_{t0}(\infty)\rangle\left[\frac{\int_0^L \Psi_{t0}(z)dz}{\int_0^\infty \Psi_{t0}(z)dz}\right] \equiv C_1\int_0^L \Psi_{t0}(z)dz, \quad (31)$$

where C_1 is a thickness-independent constant. This expression can now be substituted into Eq. (27) for the effective relaxation time constant:

$$\frac{1}{\tau_M} \equiv \frac{1}{\tau_2} + (B_{21}/2c)C_1\int_0^L \Psi_{t0}(z)dz. \quad (32)$$

Finally, the expression for the measured LUM signal becomes

$$S(\omega) = \text{const}\,\langle N_{21}(\omega)\rangle \quad (33)$$

and Eq. (29) must be used.

C. Photon density field

According to Eq. (2), $\Psi_t(z) = \Psi_d(z) + \Psi_c(z)$. The coherent component of the optical field in the bone matrix is represented by an exponentially decaying function in the direction of the incident laser energy [19],

$$\Psi_c(z) = I_0(1 - R)\exp(-\mu_t z), \quad (34)$$

where R is the Fresnel reflection coefficient of the surface and $\mu_t = \mu_a + \mu_s$ is the optical attenuation coefficient combining the effects of both the absorption coefficient, μ_a, and the scattering coefficient, μ_s. Although more accurate models of the ballistic photon field exist which describe propagation at early diffuse times [20] (corresponding to high modulation frequencies), we have found that at the relatively low frequencies involved in this work the simple exponential decay, Eq. (34), is adequate to model the frequency response of the

system. Besides, the high scattering coefficients measured in the experiments render the ballistic photon contributions negligible. The diffuse component of the photon field is described [21] by the boundary value problem of the differential equation,

$$\frac{d^2}{dz^2}\Psi_d(z) - 3\mu_a\mu_t'\Psi_d(z) = -3(1-R)I_0\mu_s(\mu_t+\mu_a g)\exp(-\mu_t z), \quad (35)$$

and the boundary conditions of optical flux continuity at surfaces at $z=0, L$:

$$\Psi_d(0) - A\frac{d}{dz}\Psi_d(z)\big|_{z=0} = 0, \quad (36a)$$

$$\Psi_d(L) + A\frac{d}{dz}\Psi_d(z)\big|_{z=L} = 0. \quad (36b)$$

In Eq. (35), $\mu_t' \equiv \mu_a + \mu_s(1-g)$ and g is the mean cosine of the scattering angle. The particular solution is

$$\Psi_{d,p}(z) = (1-R)I_0\frac{\mu_s(\mu_t+\mu_a g)}{\mu_t'(\mu_a-\mu_t^2/3\mu_t')}\exp(-\mu_t z). \quad (37a)$$

The homogeneous solution is of the form

$$\Psi_{d,h}(z) = a\exp(Qz) + b\exp(-Qz), \quad (37b)$$

where $Q=\sqrt{3\mu_a\mu_t'}$. The integration constants a and b are determined by boundary conditions (36). Here the constant A is given as $A=\frac{2}{3\mu_t'}(\frac{1+r}{1-r})$, where r is the internal reflectance, defined as the ratio of the upward-to-downward hemispherical diffuse optical fluxes at the boundary [22,23].

It can be shown that

$$b = \frac{e^{QL}[Xe^{QL}(dY) - e^{-\mu_t L}(dZ)]}{1-X^2e^{2QL}}, \quad (38a)$$

$$a = -bX - dY, \quad (38b)$$

where

$$X = \frac{1+AQ}{1-AQ}, \quad Y = \frac{1+A\mu_t}{1-AQ}, \quad Z = \frac{1-A\mu_t}{1-AQ},$$

$$d = (1-R)I_0\frac{\mu_s(\mu_t+\mu_a g)}{\mu_t'(\mu_a-\mu_t^2/3\mu_t')}. \quad (38c)$$

Combining both the particular and homogeneous solutions, the total photon density field expression describing the optical field in the bone matrix in Eqs. (32) and (33) becomes

$$\Psi_t(z) = ae^{Qz} + be^{-Qz} + [d+(1-R)I_0]e^{-\mu_t z}. \quad (39)$$

III. MATERIALS AND METHODS

The cortical layer of human skull bones was stripped off its trabecular underlayer and chosen for this study because of its mechanical strength which allowed filing its thickness down to 1.2 mm without crumbling. The skull samples used for this study were harvested from a cadaver from the Toronto General Hospital. They were stored in a container filled with saline solution when they were not in use. The saline solution was used to prevent the bone samples from developing cracks due to excessive dryness. Before the start of an experiment, a sample was removed from the storage container and was dried using a piece of paper towel. It was then left out to dry and thermalize at the ambient temperature for approximately 20 min before commencing measurements. This procedure ensures that the presence of water inside the bone does not affect the optical properties of the sample and also minimizes the influence of temporal variations of the dc temperature on the measured LUM signal. A photograph of a typical skull sample is shown in Fig. 4. Skull bones were attached to LEGO™ blocks using multipurpose epoxy (5 min Epoxy, Lepage). The block was then snapped on a LEGO™ block holder fastened to the circular rotational stage that enables rotation around the z axis. The holder was mounted on a micrometer stage. This configuration allowed the small skull samples to translate in three orthogonal directions and rotate around the vertical axis (z direction). These four degrees of freedom enable the accurate control and the precise positioning and orientation of the skull samples. As a consequence, reproducibility of experimental data was excellent as verified by studies conducted to monitor signal variation at different regions on the sample surface and the effects of changing laser radiation incidence angle.

FIG. 4. Cortical bone from a human skull sample mounted on LEGO blocks.

A schematic representation of the experimental system is displayed in Fig. 5. The main components of the system include a low-powered semiconductor laser diode, a lock-in amplifier, a laser diode controller, an infrared detector, a photodetector, and a desktop computer. The semiconductor laser diode emitting at 659 nm (Mitsubishi ML101J27, maximum power: 120 mW) with a beam diameter of 0.5 mm was used as the sample excitation source. During an experiment, the

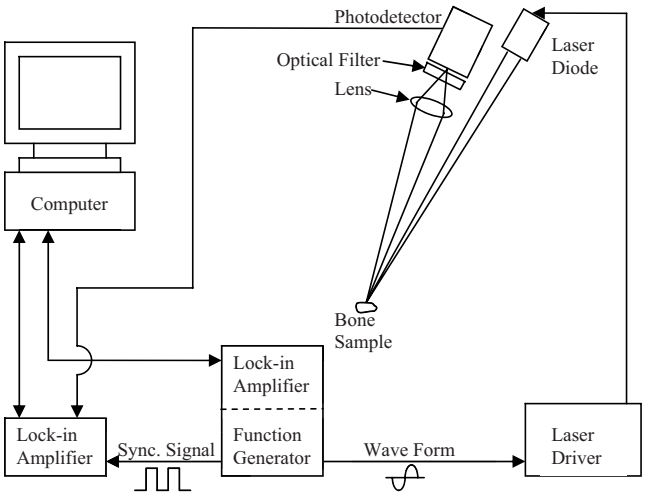

FIG. 5. Experimental setup for modulated luminescence of bones.

computer sends a frequency command to the lock-in amplifier (Stanford Research Systems, Model SR830), which generates and sends a sinusoidal voltage at that frequency to the laser diode controller (Thorlab, LDC 210 C). The sinusoidal voltage received by the laser diode controller is then transformed into a sinusoidal current which is used to modulate the intensity of the laser diode output. A fraction of the optical energy incident on the sample is absorbed and radiatively converted by the sample which emits diffuse luminescence (LUM). For the measurement of LUM signals, a focusing lens (focal length: 8 cm) and a silicon photodiode were used. A cut-on colored glass filter (Oriel 51345, cut-on wavelength: 715 nm) was placed in front of the luminescence photodetector to block off laser light radiation reflected or scattered by the bone. The possibility of laser light leakage through, or luminescence emission by, the filter itself in the presence of the impinging laser beam was considered but no detectable signal could be observed in the lock-in amplifier (EG&G model 5210). The modulated LUM signal generated by the bone was sent to the lock-in amplifier and the demodulated output signal (amplitude and phase) was processed by the desktop computer. The lock-in amplifier was controlled by home-made MATLAB-based software applications via a GPIB card (National Instruments). To account for the instrumental transfer function, a small fraction of the incident laser radiation was allowed to impinge on the photodetector and the frequency dependence of the response was recorded and stored in the computer as the reference signal. All skull measurements were normalized by the reference amplitude through division and by the phase through subtraction.

The purpose of the first series of experiments conducted with human skull bones was to evaluate the penetration depth of the diffuse luminescence field generated by the total (coherent and diffuse) photon density field in the bone created by the incident laser radiation. The extent of LUM signal penetration depth was tested by measuring the signal, painting the back surface with black paint, remeasuring and comparing the LUM signals with and without the paint layer. This procedure was repeated several times following the filing off of approx 1 mm thickness after each set of measurements.

The second type of experiments carried with a skull bone was measurements testing the effects of changing laser intensity on the frequency dependence of the LUM signal. For those experiments, a variable neutral density filter (Newport, 960-RC) was added in front of the laser diode to control the laser intensity impinging on the bone. The laser power transmitted through four filter positions was measured by a power meter (Melles Griot, power/energy meter 13PEM001). The entire scan procedure was automated and the modulation frequency and lock-in amplifier sensitivities were adjusted automatically by our MATLAB program.

IV. RESULTS

Tests were conducted to investigate the influence of hydration level on the LUM signal. It was found that LUM is relatively insensitive to changes in hydration level. There was a slight increase in phase lag with decreasing hydration level but overall the influence was minimal. Figure 6 shows the frequency scan results with and without the back-surface paint layer. It was found that LUM amplitude decreases with the black layer present, as expected from the enhanced absorption of the luminescence and/or excitation photons by the paint at the back interface. The LUM phase lag increased with the black paint thus indicating that the observed effects were not a simple change in the LUM field density in the body of the skull bone, but rather the interaction of the LUM field with the chromophore(s) responsible for the generation of luminescence. In Fig. 6 results for thicknesses above 3.2 mm are not shown since those scans were insensitive to the application of black paint. Therefore, it can be concluded that cortical skull bone of thickness higher than 3–4 mm is effectively optically semi-infinite but higher depth resolution may be obtained with higher fluence lasers. Nevertheless, following the photophysical analysis of the frequency scans, it will be seen that the LUM decay (relaxation) lifetime is a substantially more sensitive thickness probe than the presence of the back-surface paint layer.

Figure 7 shows the dependence of the LUM frequency scans on laser power (intensity). It is seen that an increase in laser power increases the LUM amplitude, as expected, but not equally at all modulation frequencies. High frequencies increase proportionately more than low frequencies. Correspondingly, the LUM phase lags decrease with increasing power and the minimum shifts to higher frequencies. At the highest frequencies the phase lags converge to essentially the same value. Experiments conducted as a function of modulation frequency with thickness as a parameter yielded results very similar to those of Fig. 6. The salient features were that LUM amplitude decreases and phase lag increases with decreasing sample thickness. The LUM amplitude decrease for thinner bone can be understood within the framework of the two mechanisms discussed above: by a larger portion of the laser energy being transmitted directly through the bone rather than becoming absorbed and internally converted to luminescence radiation and by the smaller total number of backscattered photons in the turbid medium.

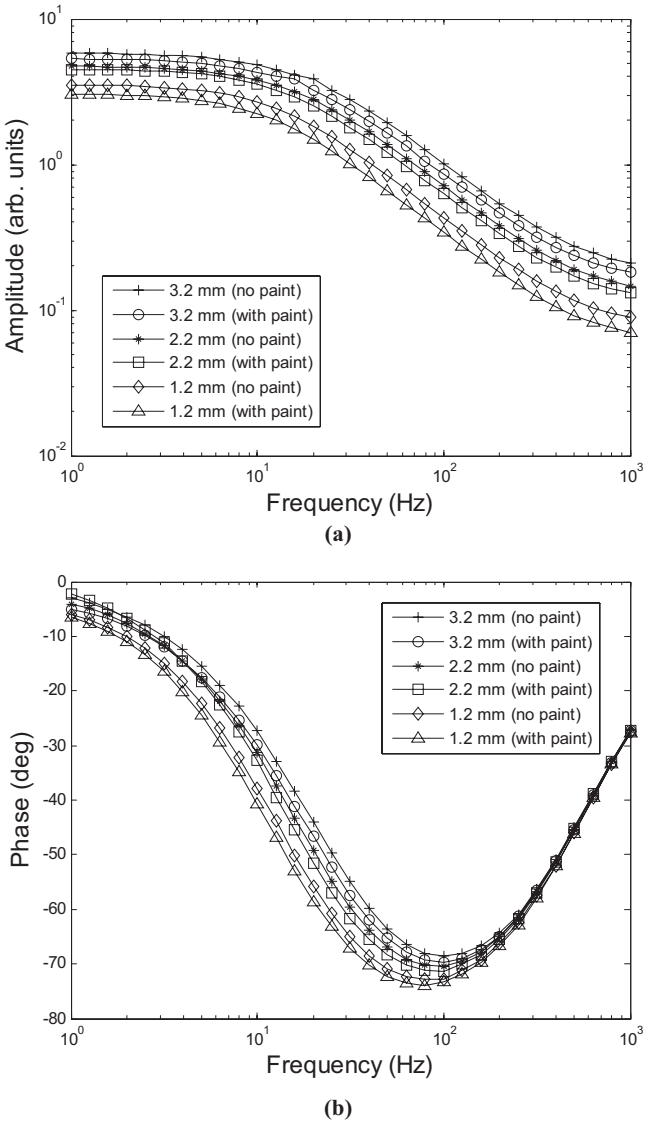

FIG. 6. LUM amplitude (a) and phase (b) frequency scans for various skull bone thicknesses with and without the presence of a back-surface black paint layer. The continuous lines are theoretical best fits to the experimental curves. Extracted effective lifetimes, τ_M=9.167 ms (L=3.2 mm, no paint); 9.381 ms (L=3.2 mm, with paint); 10.33 ms (L=2.2 mm, no paint); 11.09 ms (L=2.2 mm, with paint); 13.01 ms (L=1.2 mm, no paint); 14.18 ms (L=1.2 mm, with paint).

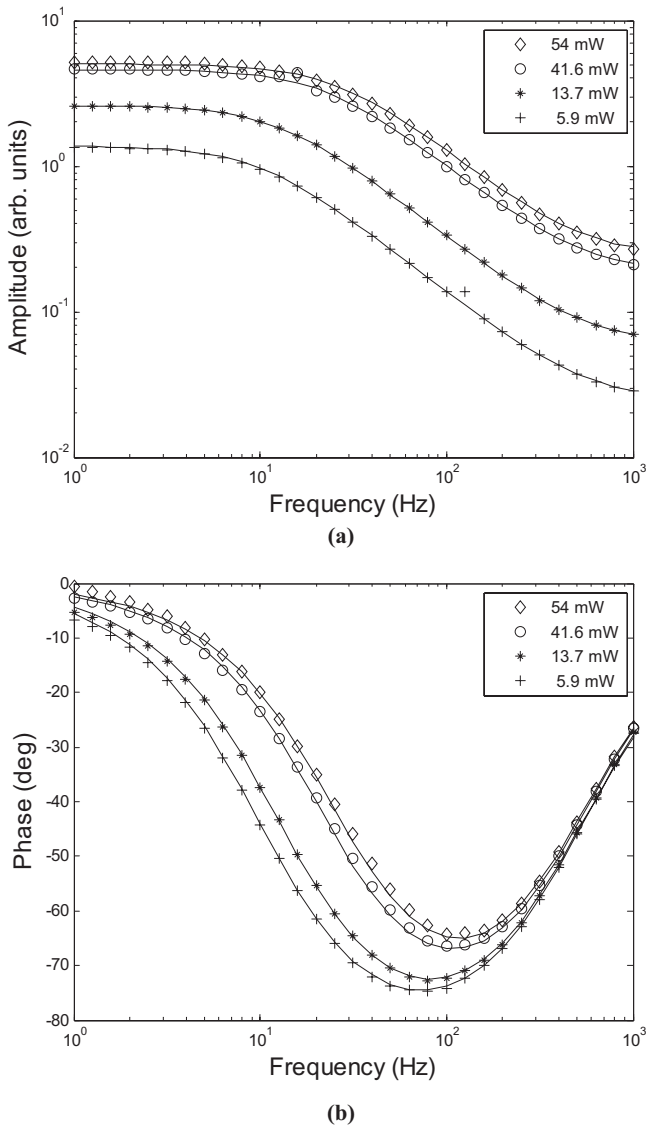

FIG. 7. LUM amplitude (a) and phase (b) frequency scans for various incident laser beam powers: 54, 41.6, 13.7, and 5.9 mW. The continuous lines are theoretical best fits to the experimental curves.

V. DISCUSSION

The theory developed in Sec. II has been applied to the interpretation of the behavior of laser-irradiated cortical skull bone observed in Fig. 6 (without back paint) and Fig. 7 and has been used to extract optical properties of the bone as well as physical quantities associated with the coupling of the optical field to the molecular excitation process of the luminescent chromophore. The theoretical model has also been found to be consistent with the sample LUM behavior in the presence of back-surface paint shown in Fig. 6.

A. Lifetime dependence on laser intensity

The effective relaxation time constant $\tau=\tau(I_0,L)$ as shown in Eq. (32) involves an integral which can be calculated from Eq. (39) as follows:

$$\int_0^L \Psi_t(z)dz = \frac{a}{Q}(e^{QL}-1)+\frac{b}{Q}(1-e^{-QL}) + \frac{[d+I_0(1-R)]}{\mu_t}(1-e^{-\mu_t L}). \quad (40)$$

The frequency dependence of the amplitude and phase of the LUM signal in Figs. 6 and 7 can be fitted to the theoretical expression (33) using Eqs. (28) and (40). Since the photon field $\Psi_{t0}(z)$ linearly depends on the incident laser intensity I_0, the dependence of $1/\tau(I_0,L)$ on this quantity is also expected to be linear. The experimental LUM amplitude and

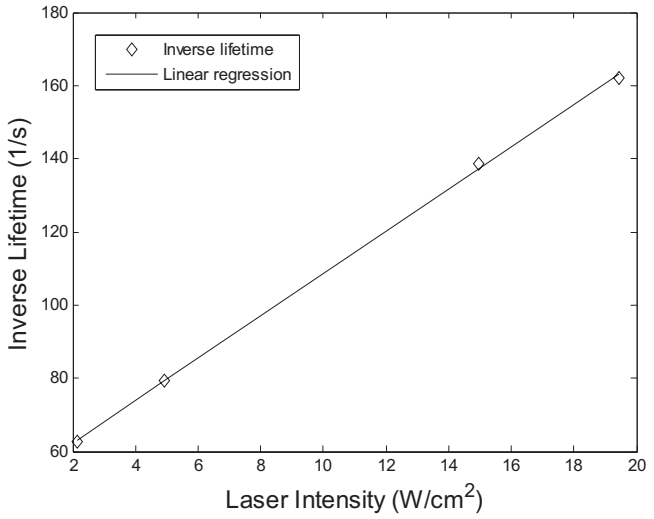

FIG. 8. Inverse effective lifetime $\tau_M^{-1}(I_0,L)$ vs I_0.

phase curves for the various laser intensities in Fig. 7 were fitted to the theoretical frequency dependence, Eq. (33), and values of the effective lifetime τ_M were extracted. These best fits are shown in Fig. 8. Table I summarizes the fitted results. Figure 8 is a plot of the inverse lifetime vs I_0. The degree of linearity of this dependence is excellent ($R=0.9996$), in agreement with Eq. (32). Using linear regression, the values of $\tau_2=19.7$ ms and $(B_{21}/2c)C_1\int_0^L \Psi'_{t0}(z)dz=5.78$ cm^2/J were determined, where $\Psi'_{t0}(z)=\frac{\partial}{\partial I_0}\Psi_{t0}(z)$ is the slope of the straight line in Fig. 8 and is equal to $\Psi_{t0}(z)/I_0$. The calculated value for τ_2 is an intrinsic deexcitation lifetime for the endogenous luminescent chromophore in cortical skull bone. Generally, it may be used as a marker to identify the luminescent molecule in different types of bone. It can also be used to characterize the molecular state of the chromophore and perhaps as a quantitative health or disease marker for the bone.

The overall shapes of the frequency responses are very similar to those observed in studies of modulated luminescence of hydroxyapatite (HAp) in dental enamel [17,19,24–26]. Modulated luminescence emission from dental enamel HAp is known to exhibit at least two decay lifetimes [17], with $\tau_2 \approx 2.1$ ms and $\tau_1 \approx 2.8$ μs. The shorter lifetime would not be observable within the limited frequency range of our skull bone experiments (1 Hz–1 kHz). In bone, it is well known that substitutional (impurity) ions into the calcium sites of the HAp lattice [2], with concomitant changes in the bone crystal size and demineralization,

TABLE I. Extracted effective lifetimes τ_M for various laser intensities.

Laser power (mW)	Laser intensity (W/cm^2)	Extracted lifetime (ms)
5.9	2.125	15.990
13.7	4.934	12.590
41.6	14.981	7.214
54.0	19.447	6.167

affect the optical scattering and absorption coefficients of bones [4,6]. This close similarity may possibly point to a connection of the endogenous chromophore responsible for the observed strong luminescence emission in cortical skull bone to HAp crystals known to be contained in the bone along with collagen [6]. A difficulty for this assignment is the effective order of magnitude difference in the extracted lifetimes from skull bone (6–16 ms, Table I) and that for dental enamel HAp (2.1 ms) [17]. It is possible that the different chemical structure of skull bone HAp and/or the presence of other constituents such as collagen may have a strong effect on the LUM relaxation response of cortical bone HAp, affecting the relaxation lifetime. Similar relaxation perturbation phenomena are widely known to occur in inorganic solid-state luminescent materials under the name "crystal-field effects" when substitutional atomic or ionic impurities alter the internal potential fields responsible for emission and shift values of radiative lifetimes. Additional similarities between HAp and skull bone optical properties have been found and are discussed below (Sec. V B).

The effective lifetime decrease with optical field intensity increase in the bone matrix reveals the type of photophysical interaction mechanism between luminescence photons and chromophore excited state. In this picture the presence of a LUM photon in the vicinity of a luminescent molecule in the upper (excited) state increases the probability for inducing the molecular decay into the lower state. This probability increases with photon density. This mechanism is also consistent with the back-surface paint results in Fig. 6. The LUM density (and amplitude) decreases due to enhanced absorption of incident photons by the paint layer, photons which otherwise would have been backscattered into the bone matrix. The decreased photon density eliminates some induced decays of the photoexcited fluorophore, resulting in longer effective lifetimes, as observed from the theoretical best fitting of Eq. (33) to the various bone-thickness data of Fig. 6 with and without the black paint layer. The LUM signal dependence on laser intensity and the calibration of bone LUM signals with respect to it by means of effective lifetime measurements is an important mechanism to consider when using this technique to study detailed optical interactions of laser fields with chromophores in the bone structure and extract intrinsic and effective lifetimes.

B. Lifetime dependence on skull bone thickness

Using the same procedure, the LUM amplitude and phase experimental curves from skull thickness studies, Fig. 6 and data from additional thicknesses (4.2, 5.2, and 6.2 mm; not shown), were fitted to Eq. (33) to extract the effective lifetime, τ as a function of thickness L. The best fits for the thinner slices are shown in Fig. 6 and extracted effective lifetimes for all thicknesses are listed in Table II. It is clearly seen that LUM effective lifetime measurements are sensitive to bone thickness as large as 6.2 mm and beyond, while the application of black paint on the back surface does not affect the depth-integrated LUM signal for thicknesses more than 3–4 mm, Fig. 6. To understand the effective lifetime dependence on the thickness of the sample, the integral $\langle \Psi_{t0}(L) \rangle$

TABLE II. Extracted effective lifetimes τ_M for various skull bone thicknesses.

Thickness (mm)	Extracted lifetime (ms)
6.2	7.132
5.2	7.141
4.2	7.439
3.2	9.167
2.2	10.330
1.2	13.006

$=C_1\int_0^L \Psi_{t0}(z)dz$ must be computed. In the previous case, Sec. V A, there was no need for this detailed calculation as the I_0 dependence can be separated out of the integrand and is always linear, while the rest of the integral is carried along as a constant. Several simulations were performed with $C_1=1$ for simplicity. Selected results are shown in Fig. 10. The family of curves shown in that figure has fixed value of μ_a and three different values of μ_s. It is seen that increasing μ_s decreases the value of the integral for large thicknesses, as expected, since less photon flux can reach deeper inside the turbid bone matrix under enhanced scattering. Nevertheless, for very thin layers ($L<1.3$ mm), the trends are nonmonotonic because the value of the integral depends on trade-offs between photon losses through the front and back surfaces (low μ_s) and photon density enhancement through multiple interreflections and/or backscattering at those surfaces. Figure 9 also shows that the integral tends to saturate with increasing thickness: the higher the value of μ_s, the smaller the saturation thickness value. This is due to the strong attenuation of the photon field at large depths which then contribute little or nothing to the integral. For smaller values of μ_s the photon field density is larger at deeper locations in the bone matrix, thus contributing larger values to the integral. Other simulations showed that the value of the integral decreases substantially with increasing μ_a, as expected from the greater

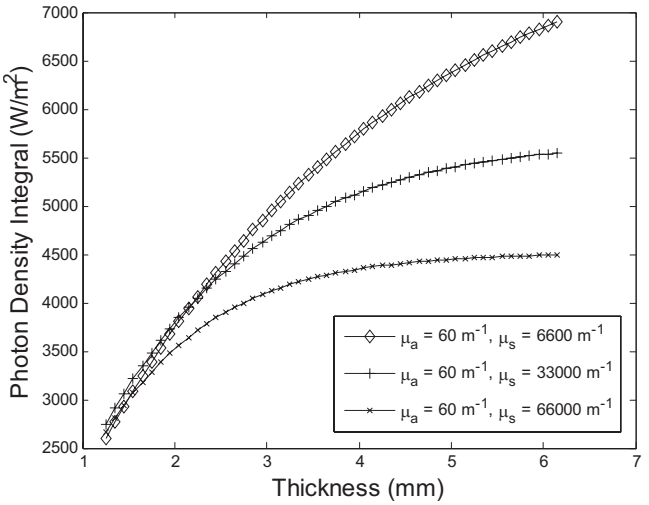

FIG. 9. Photon density integral $\int_0^L \Psi_{t0}(z)dz$ with μ_a and μ_s values as parameters.

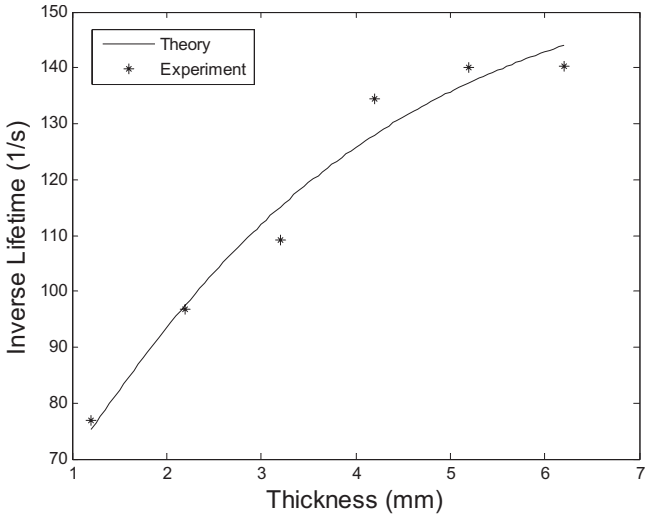

FIG. 10. Inverse effective lifetime $\tau_M^{-1}(I_0,L)$ as a function of bone thickness L.

photon loss to the bone matrix as a result of enhanced absorption. Physical consequence of these simulations is that a thicker medium captures a higher number of incident photons, thus contributing to higher cumulative LUM signal amplitude, as shown in Fig. 6(a). Another expectation is that more induced excited-state decay events will occur in a thicker matrix, thus producing a larger density of luminescence photons contributing to an enhanced mean decay rate of the chromophores and a shorter effective lifetime, τ as per the theoretical mechanism of Sec. II. This expectation was borne out using the extracted values of τ in Table II in a plot of the inverse effective lifetime vs thickness shown in Fig. 10. Equation (32) was used to fit the data to the theory. As expected, τ decreases with increasing L. The simplex downhill multiparameter fitting algorithm was used to determine the best-fitted optical absorption and scattering coefficients and $(B_{21}/2c)C_1$ values [27].

In many multiparameter fitting problems, the solution set may contain parameter values that give the best agreement between the theoretical and experimental curves mathematically but are physically invalid. To solve this difficulty, the down-hill simplex algorithm was modified so that the fitted parameters only varied within a set range of values. Based on literature values, μ_s was allowed to vary between 25 000 and 45 000 m^{-1} while μ_a varied from 2 to 80 m^{-1}. Using this enhanced algorithm, the optimal values of $(B_{21}/2c)C_1$, μ_s, and μ_a were found to be 0.0079 m/J, 44 340 m^{-1}, and 13 m^{-1}, respectively. The best-fitted curve is plotted on Fig. 10. The aforementioned μ_s and μ_a values for laser excitation at 659 nm are comparable to $\mu_s \sim 35\,000$ m^{-1} and $\mu_a \sim 60$ m^{-1} reported for horse-leg bones by Ugryumova *et al.* [6] who attributed these values to the presence of HAp crystals in the bone, and $\mu_a \sim 9-13$ m^{-1} reported for human calcaneus by Cubbedu *et al.* [28]

The foregoing interpretation of the experimental results in terms of chromophore photophysics can be used to estimate the value of the mean optical coupling coefficient B_{21}, assuming the extinction depth to be defined as the depth beyond which diffuse luminescence attenuates adequately so

that the sample is essentially semi-infinite for all larger thicknesses. This defines the luminescence saturation length L_{sat}. Our frequency scans with cortical bone thicknesses larger than those shown in Fig. 6, both amplitude and phase, showed that $L_{sat} \approx 5.2$ mm. Using Eqs. (30) and (31), $D \approx L_{sat} = 1/C_1$ or $C_1 = 192$ m. Therefore, from the best-fit values in Fig. 10 we find $B_{21}/2c = 4.1 \times 10^{-5}$ m^2/J. Assuming the refractive index of bone to be approx 1.55 [29] we obtain $B_{21} = 1.6 \times 10^4$ $m^3\ J^{-1}\ s^{-1}$. Like the calculated value of the intrinsic lifetime τ_2, this value represents a photophysical marker of the interaction between the laser generated LUM photon field in the bone matrix and the endogenous luminescent chromophore, so it is molecular species specific and can be used for monitoring bone structure at the molecular level.

A final comment can be made regarding the potential of modulated luminescence lifetime markers for clinical *in vivo* detection of BMD with the presence of an overlying skin layer. LUM is a method which is based on direct near-infrared radiative photon emissions from hard tissue chromophores. Optical absorption depth in soft tissue in the near-infrared (NIR; 650–1000 nm) spectral range is largely determined by that of water [30] and can be large (ca. 10 mm at 700 nm). However, scattering controls the overall optical attenuation [19]. These facts imply that a relatively small number of incident NIR photons have the ability to penetrate deeply into human tissue overlying bone structures and to interact with bones. Similarly, the bone luminescence thus generated in the 700–850 nm range, although strongly scattered by overlying tissue, has approx 1.0 cm optical absorption length. This means that laser-source-filtered LUM can be easily detected using synchronous lock-in detection and sensitive state-of-the-art photodetectors, e.g., Si or InGaAs, as in the experimental configuration of Fig. 5, or even photomultipliers (e.g., Hamamatsu NIR photomultiplier model H9170–75) for cases of deeper seated bones, like at the base of the spine or the wrist.

VI. CONCLUSIONS

A photophysical theory of modulated diffuse luminescence (LUM) of bones was developed and used to interpret associated measurements performed on the cortical layer of human skull bones. The purpose of the study was to assess the feasibility of applying LUM as a marker for BMD measurements for monitoring the onset of osteoporosis. The theory was based on a general excited-state manifold of the chromophore molecules constructed on the basis of experimental behavior and leading to a set of optical excitation and decay rate equations of the luminescent chromophores in the bone and on the photophysical molecular interactions with the photon field in the matrix of the bone. An effective depth-dependent relaxation lifetime $\tau(z)$ (and its mean value τ_M) of skull cortical bone was derived theoretically and was found to depend on the photon field density, as well as on the thickness of the bone. A linear dependence of τ_M on laser beam intensity, I_0, was found and sensitivity of the value of τ_M to bone thickness, L, was observed for $L \leq 6.2$ mm. Both I_0 and L experimental dependencies were in excellent agreement with the theoretical model. The values of optical absorption and scattering coefficients of the endogenous chromophore in the bone matrix at the excitation wavelength were calculated from plots of $\tau(I_0, L)$ vs laser intensity and bone thickness. The values of the coupling coefficient B_{21} and the intrinsic lifetime of the chromophore were also measured. Using similarities between skull bone LUM frequency responses, both amplitude and phase, and the frequency responses of dental LUM generated by enamel HAp, as well as the reported optical properties of human and horse-leg bones, it was shown that the luminescent chromophore in cortical human skull bone may be related to the form of HAp encountered in it. However, more work remains to be done to clarify the origin of skull bone modulated luminescence, mainly at the spectroscopic level, which can be aided by the application of the theory developed in this paper.

In summary, quantitative LUM can be used as a sensitive method to measure optical properties of the active chromophore in cortical skull bones and the optical-field-induced molecular interaction parameter, potentially as markers of bone health or disease, such as osteoporosis or cancer. When calibrated vs laser intensity, the LUM technique can also be used to measure human skull thickness. More LUM studies involving tissue-covered bones are underway to assess the technique's clinical relevance and sensitivity to BMD in the presence of a skin overlayer.

ACKNOWLEDGMENTS

The support of the Natural Sciences and Engineering Research Council with a Discovery Grant and of the Ontario Ministry of Research and Innovation with a Discovery Award in Science and Engineering (2007) granted to A. Mandelis are gratefully acknowledged.

[1] P. A. Torzilli, A. H. Brustein, K. Takebe, J. C. Zika, and K. G. Heiple, in *Mechanical Properties of Bone*, edited by S. C. Cowin (Am. Soc. Mech. Eng., New York, 1980), pp. 145–161.
[2] M. J. Glimcher, *Disorders of Bone and Mineral Metabolism* (Raven Press, New York, 1992), pp. 265–286.
[3] A. Klibanski *et al.*, JAMA, J. Am. Med. Assoc. **285**, 785 (2001).
[4] L. M. Miller, R. Huang, M. R. Chance, and C. S. Carlson, Synchrotron Radiat. News **12**, 21 (1999).
[5] A. Takeuchi, R. Araki, S. G. Proskurnin, Y. Takahashi, Y. Yamada, J. Ishi, S. Katayama, and A. Itabashi, J. Bone Miner. Res. **12**, 261 (1997).
[6] N. Ugryumova, S. J. Matcher, and P. Attenburrow, Phys. Med. Biol. **49**, 469 (2004).
[7] A. M. Coats, D. W. L. Hukins, C. T. Imrie, and R. M. Aspden, J. Microsc. **211**, 63 (2003).
[8] J. A. Kanis *et al.*, Osteoporosis Int. **4**, 368 (1994) and references therein.

[9] S. R. Cummings *et al.*, Osteoporosis Int. **8**, S1 (1998).
[10] R. D. Speller, G. J. Royle, and J. A. Horrocks, J. Phys. E **22**, 202 (1989).
[11] H. K. Genant, K. Engelke, T. Fuerst, C.-C. Gluer, S. Grampp, S. T. Harris, M. Jergas, T. Lang, Y. Lu, S. Majumdar, A. Mathur, and M. Takada, J. Bone Miner. Res. **11**, 707 (1996).
[12] G. Guglielmi, S. K. Grimston, K. C. Fischer, and R. Pacifici, Radiology **192**, 845 (1994).
[13] *Bone Densitometry and Osteoporosis*, edited by H. Genant, G. Guglielmini, and M. Jergas (Springer-Verlag Telos, New York, 1997).
[14] M. A. Hakulinen, J. S. Day, J. Toyras, M. Timonen, H. Kroger, H. Weinans, I. Kiviranta, and J. S. Jurvelin, Phys. Med. Biol. **50**, 1629 (2005).
[15] P. Laugier, in *Proceedings of the 148th Meeting of the Acoustical Society of America, San Diego, CA, 2004, Topocal Meeting Ultrasound Characterization of Cancellous and Cortical Bone, Paper 1pBB1* (unpublished).
[16] C.-H. Kwan, A. Matvienko, and A. Mandelis, in *Proceedings of SPIE BiOS Conference "Photons plus Ultrasound", San Jose CA, 2008* (SPIE, Bellingham, WA, 2008), 6856, paper 685625.
[17] L. Nicolaides, A. Mandelis, and S. H. Abrams, J. Biomed. Opt. **5**, 31 (2000).
[18] R. Hibst and R. Paulus, Caries Res. **33**, 295 (1999).
[19] L. Nicolaides, C. Feng, A. Mandelis, and S. H. Abrams, Appl. Opt. **41**, 768 (2002); A. Mandelis and C. Feng, Phys. Rev. E **65**, 021909 (2002).
[20] F. Liu, K. M. Yoo, and R. R. Alfano, Opt. Lett. **19**, 740 (1994); M. E. Zevallos L., S. K. Gayen, M. Alrubaiee, and R. R. Alfano, Appl. Phys. Lett. **86**, 011151 (2005).
[21] A. Mandelis, *Diffusion-Wave Fields: Mathematical Methods and Green Functions* (Springer-Verlag, New York, 2001, Chap. 10; A. Ishimaru, Y. Kuga, R. L. T. Cheung and K. Shimizu, J. Opt. Soc. Am. **73**, 131 (1983); M. A. O'Leary, D. A. Boas, X. D. Li, B. Chance, and A. G. Yodh, Opt. Lett. **21**, 158 (1996); K. Yoo and R. R. Alfano, *ibid.* **15**, 320 (1990); D. Contini, F. Martelli, and G. Zaccanti, Appl. Opt. **36**, 4587 (1997).
[22] R. R. Anderson, H. Beck, U. Bruggemann, W. Farinelli, S. L. Jacques, and J. Parrish, Appl. Opt. **28**, 2256 (1989).
[23] R. A. Groenhuis, H. A. Ferwerda, and J. J. T. Bosch, Appl. Opt. **22**, 2456 (1983).
[24] A. Mandelis, in *Proceedings of SPIE Thermosense XXIV, Orlando, 2002*, edited by X. P. Maldague and A. E. Rozlosnik (SPIE, Bellingham, WA, 2002), Vol. 4710, p. 373.
[25] R. J. Jeon, C. Han, A. Mandelis, V. Sanchez, and S. H. Abrams, Caries Res. **38**, 497 (2004).
[26] R. J. Jeon, A. Mandelis, V. Sanchez, and S. H. Abrams, J. Biomed. Opt. **9**, 804 (2004).
[27] W. H. Press, S. A. Teukolsky, W. T. Wetterling, and B. P. Flannery, *Numerical Recipes in Fortran*, 2nd ed. (Cambridge University Press, New York, 1992), Chap. 10.4.
[28] R. Cubbedu, E. Giambattistelli, A. Pifferi, P. Taroni, and A. Torricelli, *In-vivo Optical Biopsy of the Calcaneous: A Novel Diagnostic Tool for Osteoporosis*, Proceedings of the Second Joint EMBS/BMES (Engineering in Medicine and Biology Society/Biomedical Engineering Society) Conference, Houston, TX (IEEE Press, New York, 2002), Vol. 3, pp. 2247–2248.
[29] A. Ascenzi and C. Fabry, J. Biophys. Biochem. Cytol. **6**, 139 (1959).
[30] S. Prahl, "Optical absorption coefficient of water,".http://omlc.ogi.edu/spectra/water/index.html